



UNIVERSITY OF LEEDS

This is a repository copy of *Designer Multimode Localized Random Lasing in Amorphous Lattices at Terahertz Frequencies*.

White Rose Research Online URL for this paper:
<http://eprints.whiterose.ac.uk/109963/>

Version: Accepted Version

Article:

Zeng, Y, Liang, G, Liang, HK et al. (11 more authors) (2016) Designer Multimode Localized Random Lasing in Amorphous Lattices at Terahertz Frequencies. *ACS Photonics*, 3 (12). pp. 2453-2460. ISSN 2330-4022

<https://doi.org/10.1021/acsp Photonics.6b00711>

© 2016 American Chemical Society. This document is the Accepted Manuscript version of a Published Work that appeared in final form in *ACS Photonics*, copyright © American Chemical Society after peer review and technical editing by the publisher. To access the final edited and published work see <https://doi.org/10.1021/acsp Photonics.6b00711>.
Uploaded in accordance with the publisher's self-archiving policy.

Reuse

Unless indicated otherwise, fulltext items are protected by copyright with all rights reserved. The copyright exception in section 29 of the Copyright, Designs and Patents Act 1988 allows the making of a single copy solely for the purpose of non-commercial research or private study within the limits of fair dealing. The publisher or other rights-holder may allow further reproduction and re-use of this version - refer to the White Rose Research Online record for this item. Where records identify the publisher as the copyright holder, users can verify any specific terms of use on the publisher's website.

Takedown

If you consider content in White Rose Research Online to be in breach of UK law, please notify us by emailing eprints@whiterose.ac.uk including the URL of the record and the reason for the withdrawal request.



eprints@whiterose.ac.uk
<https://eprints.whiterose.ac.uk/>

Designer Multimode Localized Random Lasing in Amorphous Lattices at Terahertz Frequencies

Yongquan Zeng¹, Guozhen Liang¹, Hou Kun Liang², Shampy Mansha³, Bo Meng¹, Tao Liu¹, Xiaonan Hu¹, Jin Tao¹, Lianhe Li⁴, Alexander Giles Davies⁴, Edmund Harold Linfield⁴, Ying Zhang², Yidong Chong³, and Qi Jie Wang^{1,3,*}

¹ *Centre for OptoElectronics and Biophotonics, School of Electrical and Electronic Engineering & The Photonic Institute, Nanyang Technological University, 50 Nanyang Avenue, Singapore 639798, Singapore*

² *Singapore Institute of Manufacturing Technology, 2 Fusionopolis Way, Singapore 138634, Singapore*

³ *School of Physical and Mathematical Sciences, Nanyang Technological University, 21 Nanyang Link, Singapore 637371, Singapore*

⁴ *School of Electronic and Electrical Engineering, University of Leeds, Leeds LS2 9JT, UK*

Abstract

Random lasers are a special class of laser in which light is confined through multiple scattering and interference process in a disordered medium, without a traditional optical cavity. They have been widely studied to investigate fundamental phenomena such as Anderson localization, and for applications such as speckle-free imaging, benefitting from multiple lasing modes. However, achieving controlled localized multi-mode random lasing at long wavelengths, such as in the terahertz (THz) frequency regime, remains a challenge. Here, we study devices consisting of randomly-distributed pillars fabricated from a quantum cascade gain medium, and show that such structures can achieve transverse-magnetic polarized (TM) multi-mode random lasing, with strongly localized modes at THz frequencies. The weak short-range order induced by the pillar distribution is sufficient to ensure high quality-factor modes that have a large overlap with the active material. Furthermore, the emission spectrum can be easily tuned by tailoring the scatterer size and filling fraction. These “designer” random lasers, realized using standard photolithography

techniques, provide a promising platform for investigating disordered photonics with pre-designed randomness in the THz frequency range, and may have potential applications such as speckle-free imaging.

Keywords: random laser, terahertz frequency, quantum cascade laser, multi-mode lasing, localization

INTRODUCTION

In conventional laser cavities, randomness is usually undesirable because it distorts the optical modes and leads to additional cavity loss. However, it has been recognized that a special class of laser, random lasers¹, can exhibit interesting and potentially useful properties. In random lasers, light is confined through multiple scattering and interference in a randomly-arranged scattering medium. Lasing takes place when the gain experienced by one or more of the complex modes overcomes the loss. The resulting multi-mode lasing emission spectrum has many potential applications. For example, it has been suggested that randomly-arranged nanoparticle clusters can be used for “fingerprinting” applications in document encoding and material labeling². Multi-mode random lasers can also be employed as light sources for speckle-free imaging applications, owing to the low spatial coherence of an ensemble of uncorrelated wavefronts^{3,4}. Other possible applications can be found in display lighting, tumor detection⁵ and sensing⁶.

To date, random lasing has been achieved in a wide range of media, including nanocrystalline ZnO powders^{7,8}, ceramics⁹, organic composites¹⁰ and nanoparticles (e.g., TiO₂, ZnO and GaN) dispersed in fluorescent dyes^{1,11-14}. The lasing frequencies have been demonstrated to range from

the near-ultraviolet to the mid-infrared (mid-IR)¹⁵. At lower frequencies, terahertz (THz) lasers based on quasi-periodic structures have been developed^{16,17} and a hyperuniform disordered laser has been demonstrated¹⁸.

THz frequency technology has seen impressive progress in recent years. Notable achievements include the invention and advancement of THz quantum cascade lasers (QCLs)^{19,20}, sensitive THz photodetectors^{21,22}, and THz modulators^{23,24}. THz QCLs are electrically-pumped semiconductor-based lasers based on electronic transitions between the subbands of a quantum well superlattice¹⁹. They can serve as compact, high intensity THz sources, with applications in, for example, non-invasive parallel imaging^{25,26}. Such applications would particularly benefit from a laser with low spatial coherence, as this would improve the image quality through the reduction of coherent artefacts.

Here, we report on the development of surface-emitting, multi-mode THz random QCLs comprising dielectric pillars arranged in a two-dimensional (2D) amorphous lattice²⁷. These QCLs are electrically pumped, and emit in the transverse-magnetic (TM) polarization due to inter-subband selection rules²⁸. Compared to air hole scatterers (which were exploited in a previously-demonstrated mid-IR random QCL¹⁵), isolated dielectric pillars have superior scattering efficiency for TM polarized light²⁹. In our structure, this leads to a substantial Q factor enhancement of localized modes near the edge of the TM gap. The pillars are formed by dry etching the quantum cascade active material, and serve not only as in-plane scatterers but also as the gain medium. Strongly localized multi-mode random lasing was observed at around 3.3 THz, with more than 13 lasing modes. Furthermore, we demonstrate that the lasing frequency can be fine-tuned by modifying structural parameters such as the pillar radius and the lattice filling fraction (FF).

RESULTS

Design of the 2D THz random laser

Previously, a mid-infrared random lasing was demonstrated in QCLs at $\sim 10\ \mu\text{m}$ by Liang *et al.*, through drilling randomly-distributed circular holes in a quantum cascade laser active region¹⁵. Nevertheless, this design was hampered by the weak scattering efficiency of air holes for TM modes, which limited the number of lasing modes to three. Such a scheme is therefore unsuitable for a QCL in the THz frequency range, where the gain coefficient is much lower than that of mid-IR QCLs. However, isolated dielectric pillars provide much stronger scattering efficiency than air holes for TM polarized light. Previous studies show that a strong bandgap can be supported by photonic lattices formed by isolated pillars^{30,31}. Since electrical pumping requires direct electrical contact to the pillars, we adopt a “double-metal waveguide” design, enclosing the pillars between parallel metal layers. This waveguide is commonly employed for THz QCLs, achieving near-unity vertical optical confinement, owing to the low losses of metal at THz frequencies^{32,33}.

The device design is shown in Fig. 1. Circular QC pillars, with radii of a few microns and $10\ \mu\text{m}$ height, are randomly distributed in a 2D lattice. The pillars were formed through inductively coupled plasma (ICP) etching of the THz QCL active region, and embedded in benzocyclobutene (BCB)³⁴⁻³⁷ for mechanical support. BCB is a non-conducting resin with good planarization property, low losses at THz frequencies, excellent thermo-stability, and low refractive index. The 2D scattering medium (formed by the pillars and BCB) is sandwiched between two thin layers of Ti/Au, which are used for current injection as well as vertical confinement. To allow for surface (i.e. vertical) emission, micro-apertures of $1.5\ \mu\text{m}$ radius were etched into the top plate, at the center position of each pillar. Fig. 1b and 1c show scanning electron microscope images of the

QC pillars after ICP dry etching, and of the finished device, respectively. The refractive index contrast in the scattering medium is approximately 3.6 (GaAs): 1.58 (BCB), which is higher than in many other random laser systems^{5,11,38,39}, allowing for stronger in-plane mode confinement. As the size of the output aperture on top of each pillar is in deep subwavelength regime and the lasing modes are largely anti-symmetric with respect to the apertures, only a small fraction of the light is coupled out from the laser cavity (see *SI Text*). By 3D Finite-Element-Method (FEM) simulations using Comsol Multiphysics, the vertical quality (Q) factor corresponding to the surface emission loss was estimated to be several thousand, which is relatively high as compared to in-plane Q factors including the consideration of material losses as discussed below. Thus, in the following theoretical analysis, we use 2D simplified models to approximate 3D full-structure simulations which are storage- and time-consuming.

The positions of the QC pillars are determined by a random placement algorithm, subject to the constraint of a ‘minimum center-to-center distance’: $|P_i - P_j| \geq 2r + \Delta$, where P_i and P_j are the center positions of any two pillars, r is the radius of the pillar, and Δ is the minimum edge-to-edge separation between pillars (e.g. $\Delta = 0$ means each pillar is allowed to touch another one but without overlap). The pillars are placed sequentially, with any subsequent placement rejected if it violates this constraint. The constraint introduces weak short-range order into the random structure. To qualitatively show the effects of the short-range order, the power spectra of structures with different Δ were compared. A substantial gap in the power spectrum can be found for the structure with larger Δ , as shown in Fig. 2a. The short-range order can be further enhanced for a wider bandgap by using more sophisticated placement algorithms, such as molecular dynamics-based close-packing; however, even with the present simple algorithm, the

intensity in the power spectrum spans several orders of magnitude near the gap. This can be attributed to the scattering efficiency of the dielectric pillars.

The power spectra in Fig. 2a were calculated using 2D finite-difference time-domain (FDTD) simulations, with pillars of $6.4 \mu\text{m}$ radius distributed within a $1000 \mu\text{m} \times 1000 \mu\text{m}$ area; the total FF is 36.5%. For $\Delta = 0 \mu\text{m}$ and $\Delta = 2.5 \mu\text{m}$, we observe dense peaks clustering around 3.3 THz, corresponding to multiple resonant modes. For the $\Delta = 2.5 \mu\text{m}$ case (vertically shifted down by 10^3 a.u. for clarity), there is, however, a prominent spectral bandgap. By contrast, for an air-hole structure (without pillars), the power spectrum (vertically shifted down by 10^6 a.u. for clarity) is uniform with small random peaks over a broad spectral range. As a further probe of the structure's short-range order, we calculated the spatial autocorrelation function of the ensemble, $C(\Delta r) = \langle \Theta(r)\Theta(r + \Delta r) \rangle / \langle \Theta(r) \rangle^2 - 1$, averaged over 100 independent configurations (For this calculation, we take $\Theta = 1$ inside the rods, and $\Theta = 0$ outside.). The result, shown in Fig. 2b, reveals an estimated correlation length L_c ($\sim 0.3-0.4a$) that is smaller than a (the average center-to-center distance of the pillars), obtained from an exponential fit $\exp(-\Delta r / L_c)$ of the autocorrelation curve. This indicates that the short-range order is fairly weak, compared to amorphous structures such as that in Ref. 40. Likewise, the power Fourier spectrum of the structure geometry, shown in the inset of Fig. 2b, displays a weak isotropic scattering ring around the spatial frequency $2\pi/a$.

To determine the in-plane modal quality (Q) factors, we performed 2D FEM simulations. Fig. 2c shows the in-plane Q factor of the mode in a typical structure, overlaid on the power spectrum near the gap. With the BCB loss neglected, we find a large number of modes with Q factors as high as 10^6 (indicating strong in-plane optical confinement) on either side of the gap. If a realistic

level of BCB loss is included ($\sim 11 \text{ cm}^{-1}$), the Q factors are substantially reduced; however, as shown in Fig. 2d, the band edge modes at lower frequencies of the bandgap still retain relatively high Q factors. Note also that the Q factors just below the gap ($Q \sim 1300$) are much larger than those above the gap ($Q < 300$), which can be attributed to the different spatial overlap of the modes with the BCB region, as discussed below.

Fig. 3a shows the field intensity distributions of a selection of random modes on each side of the gap (the corresponding modes are highlighted by the blue ellipses in Fig. 2c). It is noteworthy that the modes at the lower edge of the gap match well with the main emission peaks which will be shown in the results section. Due to the strong scattering efficiency, the short-range ordered amorphous structures demonstrated here support multiple localized random lasing modes, some with nearly diffraction-limited localization lengths (see *SI Text*, Fig. S1 and Fig. S2). These strongly localized modes are beneficial for emission with low spatial coherence and the realization of low-threshold lasing. Furthermore, there is a clear distinction between the modes below and above the gap: the modes below the gap are mainly concentrated in the pillars (e.g. at 3.33 THz), while the modes above the gap are mainly located in the BCB (e.g. at 3.56 THz). This explains why the latter have much lower in-plane Q factors, as seen in Fig. 2d. The high-Q modes below the gap are thus more favorable for lasing, and we shall see below that this frequency region indeed matches the distribution of the experimentally-observed emission peaks.

Comparing to the structure with $\Delta = 0 \text{ }\mu\text{m}$, the presence of a non-zero separation $\Delta = 2.5 \text{ }\mu\text{m}$ between pillar edges makes the structure more favorable for lasing. It creates a gap in the power spectrum, with more pronounced Q-factor enhancement at the band edge, as well as a larger overlap of the modes with the active region (and thus higher net gain). We can quantify this using an “overlap factor”, defined as the fraction of the field energy confined in the QC pillars:

$$\Gamma = \int_{xy=AR} \varepsilon(x, y)I(x, y)dxdy / \int \varepsilon(x, y)I(x, y)dxdy \quad (1)$$

where “AR” denotes active region, $\varepsilon(x, y)$ is the dielectric constant and $I(x, y)$ is the intensity distribution. Fig. 3b shows the overlap factor versus FF for $\Delta = 0 \mu\text{m}$ and $\Delta = 2.5 \mu\text{m}$, where each data point is averaged over 100 modes at the band edge below the gap. As expected, the overlap factors are significantly higher for the $\Delta = 2.5 \mu\text{m}$ structure. The parameter $\Delta = 2.5 \mu\text{m}$ further restricts the movement of the pillars so as to introduce a perceptible short-range order into the structure, leading to the opening of the bandgap and the enhanced Q factors at the band edges. This makes the maximum of field tend to be better confined inside the pillars for the lower band edge modes (see Fig. 2d and *SI Text*, Fig. S2), which is the reason for larger overlap factors and higher Q factors.

Characterization results

The THz QCL wafer used here was based on a three-well resonant-phonon GaAs/Al_{0.15}Ga_{0.85}As design⁴¹, with gain centered around 3.1 THz. Based on the random QCL design described above, we fabricated a variety of structures with different pillar sizes and FFs. As a reference, we also fabricated and characterized double-metal ridge lasers on the same QC wafer, with width 106 μm and length 2 mm. All the devices were driven by a pulser with a repetition rate of 10 kHz and a pulse width of 500 ns.

Fig. 4a shows the LIV curves of a random QCL with a pillar radius 6.4 μm , a FF of 36.5% and $\Delta = 2.5 \mu\text{m}$. The lasing threshold at 10 K is around 1.60 kA/cm^2 . This value is slightly larger than that of the ridge laser (1.33 kA/cm^2), mainly attributable to the BCB losses. Just above threshold, the light intensity increases sharply due to the rapid appearance of many modes with

comparable Q factors. The emission spectra are recorded by a FTIR with a DTGS THz detector (response time $\sim 1\text{ms}$) with a total scanning time of over 1 minute, and thus represent time averages over multiple pulses (it would be interesting to study dynamical shot-to-shot fluctuations of the lasing modes, but this would require Terahertz detectors with a much faster response time). Measured by our existing system, the spectrum and power of the device are stable during the characterization. At the rollover current density, 13 lasing peaks can be easily distinguished in the emission spectrum (Fig. 4b), measured using an FTIR resolution of 0.2 cm^{-1} ; additional peaks are likely to be resolved with a higher resolution spectral measurement. The lasing peaks occur within the range 3.1–3.4 THz, which is in good agreement with the simulation results showing that this is the frequency range where the modes are strongly localized and confined in the QC pillars (Fig. 2d and Fig. 3a). We also found experimental evidence that the lasing modes are strongly localized, by partially covering the device surface with a copper sheet, whereupon some of the peaks were greatly suppressed (due to the light emitted from the covered area not reaching the FTIR system), while other peaks were largely unaffected. For further details, see *SI Text*, Fig. S4.

In comparison to the emission spectra of a QCL ridge laser, no apparent spectral periodicity can be found in the random laser spectrum. Moreover, the dependence of the lasing spectra on applied current reveals a qualitative difference between the behavior of the random QCL and the reference ridge laser. As shown in Fig. 5a, the emission of the ridge laser is continuously blue-shifted from 3.05 THz to 3.15 THz with increasing pumping current. This is due to a blue-shift in the gain center of the QC medium, a typical feature of the three-well resonant phonon active region design employed here. By contrast, the lasing peaks of the random QCL experience negligible shift with current; the principal peaks are clustered around 3.3 THz, away from the

gain center of the QC medium. Just above the threshold current, multiple peaks appear almost simultaneously and their intensities increase monotonically with pumping current until the rollover current. This is consistent with the interpretation that the random lasing modes are determined by the high-Q band edge modes of the 2D scattering medium.

The emission characteristics of the random QCL can be tailored by changing the parameters of the underlying scattering medium, such as the size and/or the density of the scatterers. The position of short-range order induced gap is approximately inverse to the effective lattice constant $a \propto r/\sqrt{FF}$. Fig. 6a shows the simulated power spectra for structures with varying FF, as well as varying pillar radius; Fig. 6b shows the corresponding experimental emission spectra. As expected, the gap in the calculated power spectra, and the peaks in the emission spectra, both undergo blue-shifts when r is reduced with fixed FF, or when FF is increased with fixed r . The experimentally-determined spectral frequency range and their shift with r and FF agree well with the calculated high-Q band edge frequencies.

DISCUSSION AND CONCLUSIONS

We have demonstrated multi-mode random QCLs operating at THz frequencies. The fact that there are multiple modes, subject to strong localization, is highly promising for future applications; for example, these devices may be able to serve as high-intensity, low-spatial-coherence sources for speckle-free full field imaging at THz frequencies. By comparison, the previous demonstration of a random QCL (using an random air-hole design at mid-IR frequencies⁴², or using hyperuniform pillar structure design¹⁸) exhibited only 2–3 peaks in the

spectrum. Based on these results, even more strongly multi-modal behavior could be achieved in three ways: (i) by replacing the BCB with a lower-loss supporting material, such as cyclic olefin copolymer^{43,44}, which would significantly increase the modal Q factors; (ii) by connecting the pillars with dielectric veins, which would reduce or eliminate the need for the BCB support³¹; and (iii) by increasing the short-range order through more sophisticated placement algorithms, such as molecular dynamics-based jam packing, which would again increase the modal Q factors.

Our random QCLs are electrically pumped using metallic top plates, with micro-apertures for surface emission. This design feature works well at THz frequencies where metallic losses are extremely low, but may lead to unacceptably high losses if one seeks to scale these devices towards mid-IR frequencies (a frequency range with important technological applications such as molecular spectral fingerprinting). To realize a multi-mode mid-IR QCL, one promising route would be to utilize a dielectric pillar design without an enclosing metallic top plate; the pillars can be joined with dielectric veins to provide the connectivity required for electrical pumping. This has been shown theoretically to provide sufficiently high-Q modes for multi-mode lasing³¹.

We have found that the emission spectrum of the random QCLs can be easily controlled by the size and filling fraction of the scatterers, but is relatively insensitive to the pumping current. Since the individual modes appear to be quite strongly localized, this raises the interesting prospect of designing a random QCL where the scatterer parameters vary across the surface. This would lead to random lasing over a wide spectral range. **In terms of emission power, optimization work on for example the aperture size can be done to enhance the power level.**

METHODS

Device Fabrication. To fabricate the random QCLs, Ti/Au was first deposited both on top of the QCL structure and onto an n^+ doped GaAs host substrate; this was followed by Au/Au thermo-compression wafer bonding. The QCL wafer was then polished and selectively wet-etched to remove the substrate down to an etch-stop layer. Through conventional photolithography and ICP dry etching of the active region, with gas ratio (in SCCM) of $\text{Ar}/\text{Cl}_2/\text{BCl}_3 = 5/5/5$, the QCL active region was etched into pillars of the intended radius (ranging from 6–8 μm) and 10 μm height. The structure was next spin-coated with BCB (CYCLOTENE 3022-46) until the top surface was planar; the detailed BCB planarization process was the same as in Ref. 35. The BCB was then etched by reactive ion etching (RIE) with a gas ratio of $\text{O}_2/\text{CF}_4 = 25/100$ (SCCM) to expose the top surface of the QC pillars. Negative resist photolithography was conducted to define the pumping area and extraction holes on top of the pillars, followed by a 20/600 nm Ti/Au layer deposition and lift-off. Finally, a $\text{BCl}_3/\text{CH}_4/\text{Cl}_2$ RIE plasma mixture with ratio of 100/20/5 (SCCM) was used for 1 min to remove the highly-doped contact layer in the holes. This prevents the otherwise strong absorption of THz radiation, allowing it to be coupled out. The host substrate was thinned to around 180 μm and a 15/200 nm Ti/Au layer was deposited as bottom contact, before the sample were cleaved, indium-soldered onto copper submounts, wire-bonded and attached to the heatsink in a cryostat for measurement. The schematic structures of the fabrication processes of the developed terahertz quantum cascade random laser are shown in the *SI Text*, Fig. S5.

Device characterization. The fabricated 2D THz random QCLs were characterized using a Bruker FTIR with a room-temperature DTGS detector. The scanning resolution was chosen to be 0.5 cm^{-1} in normal operation, and 0.2 cm^{-1} when more accurate measurements were needed for identifying the peak number and peak positions. The devices were driven by a pulser with a

repetition rate of 10 kHz and a pulse width of 500 ns. The devices were mounted in a helium-gas-stream cryostat for cooling with temperature control.

ASSOCIATED CONTENT

Supporting Information

Supporting Information for this article is available free of charge on the ACS Publications website at DOI: xxxxx

- 1). Multiple strongly localized modes within one structure.
- 2). Vertical quality (Q) factor approximation.
- 3). Modal localization demonstration by partially covering a copper sheet above the device surface.
- 4). Schematic fabrication process for the terahertz random quantum cascade lasers.

AUTHOR INFORMATION

Corresponding Author

*E-mail (Q. J. WANG): qjwang@ntu.edu.sg

Author contribution: Y. Q. Z., G. Z. L. and Q. J. W. conceived the idea; Y. Q. Z., G. Z. L., H. K. L., M. B., X. N. H., L. H. L, A. G. D. and E. H. L. performed experiment; Y. Q. Z., G. Z. L., S. M., T. L., T. J. and Y. D. C. performed simulation and analyzed data; Y. Q. Z., G. Z. L., Y. D. C. and Q. J. W. wrote the manuscript. The authors declare no conflict of interest.

Notes

The authors declare no competing financial interest.

ACKNOWLEDGMENTS

This work is supported by Singapore National Research Foundation, Competitive Research Program (NRF2015 NRF-CRP002-008), Singapore Ministry of Education Tier 2 program (MOE2016-T2-1-128) and SERC (grant number 1426500050) from the Agency for Science, Technology and Research (A*STAR), Singapore. L. H. L, A. G. D. and E. H. L. acknowledge funding from the Engineering and Physical Sciences Research Council [EP/J017671/1, 'COTS']. S.M. and C.Y.D. acknowledge support from the Singapore National Research Foundation under grant No. NRFF2012-02. Support from the Royal Society and Wolfson Foundation is also acknowledged (<https://www.epsrc.ac.uk/about/standards/researchdata/>).

REFERENCES

- (1) Lawandy, N. M.; Balachandran, R. M.; Gomes, a. S. L.; Sauvain, E. Laser Action in Strongly Scattering Media. *Nature* **1994**, *368* (6470), 436–438.
- (2) Cao, H. Lasing in Random Media. *Waves in Random Media* **2003**, *13* (December 2013), R1–R39.
- (3) Redding, B.; Choma, M. a.; Cao, H. Speckle-Free Laser Imaging Using Random Laser Illumination. *Nat. Photonics* **2012**, *6* (June), 355–359.
- (4) Redding, B.; Choma, M. A.; Cao, H. Spatial Coherence of Random Laser Emission. *Opt. Lett.* **2011**, *36* (17), 3404–3406.
- (5) Polson, R. C.; Vardeny, Z. V. Random Lasing in Human Tissues. *Appl. Phys. Lett.* **2004**,

85 (7), 1289–1291.

- (6) Song, Q. H.; Xiao, S. M.; Xu, Z. B.; Shalaev, V. M.; Kim, Y. L. Random Laser Spectroscopy for Nanoscale Perturbation Sensing. *Opt. Lett.* **2010**, *35* (15), 2624–2626.
- (7) Cao, H.; Zhao, Y. G.; Ho, S. T.; Seelig, E. W.; Wang, Q. H.; Chang, R. P. H. Random Laser Action in Semiconductor Powder. *Phys. Rev. Lett.* **1999**, *82* (11), 2278–2281.
- (8) Cao, H.; Xu, J. Y.; Zhang, D. Z. D.; Chang, S. H.; Ho, S. T.; Seelig, E. W.; Liu, X.; Chang, R. P. H. Spatial Confinement of Laser Light in Active Random Media. *Phys. Rev. Lett.* **2000**, *84* (c), 5584–5587.
- (9) Bahoura, M.; Morris, K. J.; Noginov, M. A. Threshold and Slope Efficiency of Nd_{0.5}La_{0.5}Al₃(BO₃)₄ Ceramic Random Laser: Effect of the Pumped Spot Size. *Opt. Commun.* **2002**, *201* (4-6), 405–411.
- (10) Klein, S.; Cregut, O.; Gindre, D.; Boeglin, A.; Dorkenoo, K. D. Random Laser Action in Organic Film during the Photopolymerization Process. *Opt Express* **2005**, *13* (14), 5387–5392.
- (11) Fan, S. Z.; Zhang, X. Y.; Wang, Q. P.; Zhang, C.; Wang, Z. P. Build-up Time of the Random Laser in R6G Dye Solution with TiO₂ Scatterers. *High-Power Lasers Appl. V* **2010**, *7843*, 784314.
- (12) Leonetti, M.; Conti, C.; López, C. Dynamics of Phase-Locking Random Lasers. *Phys. Rev. A* **2013**, *88* (4), 43834.
- (13) Consoli, A.; López, C. Decoupling Gain and Feedback in Coherent Random Lasers: Experiments and Simulations. *Sci. Rep.* **2015**, *5*, 16848.
- (14) Consoli, A.; Lopez, C. Emission Regimes of Random Lasers with Spatially Localized Feedback. *Opt. Express* **2016**, *24* (10), 10912–10920.
- (15) Liang, H. K.; Meng, B.; Liang, G. Z.; Tao, J.; Chong, Y. D.; Wang, Q. J.; Zhang, Y. Electrically Pumped Mid-Infrared Random Lasers. *Adv. Mater.* **2013**, *25* (47), 6859–6863.

- (16) Mahler, L.; Tredicucci, A.; Beltram, F.; Walther, C.; Faist, J.; Beere, H. E.; Ritchie, D. A.; Wiersma, D. S. Quasi-Periodic Distributed Feedback Laser. *Nat. Photonics* **2010**, *4* (3), 165–169.
- (17) Vitiello, M. S.; Nobile, M.; Ronzani, A.; Tredicucci, A.; Castellano, F.; Talora, V.; Li, L.; Linfield, E. H.; Davies, A. G. Photonic Quasi-Crystal Terahertz Lasers. *Nat. Commun.* **2014**, *5*.
- (18) Degl’Innocenti, R.; Shah, Y. D.; Masini, L.; Ronzani, A.; Pitanti, A.; Ren, Y.; Jessop, D. S.; Tredicucci, A.; Beere, H. E.; Ritchie, D. A. Hyperuniform Disordered Terahertz Quantum Cascade Laser. *Sci. Rep.* **2016**, *6*, 19325.
- (19) Kohler, R.; Tredicucci, A.; Beltram, F.; Beere, H. E.; Linfield, E. H.; Davies, A. G.; Ritchie, D. A.; Iotti, R. C.; Rossi, F. Terahertz Semiconductor-Heterostructure Laser. *Nature* **2002**, *417* (6885), 156–159.
- (20) Williams, B. S. Terahertz Quantum-Cascade Lasers. *Nat. Photonics* **2007**, *1* (9), 517–525.
- (21) Liu, H. C.; Song, C. Y.; SpringThorpe, A. J.; Cao, J. C. Terahertz Quantum-Well Photodetector. *Appl. Phys. Lett.* **2004**, *84* (20), 4068.
- (22) Graf, M.; Scalari, G.; Hofstetter, D.; Faist, J.; Beere, H.; Linfield, E.; Ritchie, D.; Davies, G. Terahertz Range Quantum Well Infrared Photodetector. *Appl. Phys. Lett.* **2004**, *84* (4), 475–477.
- (23) Sensale-Rodriguez, B.; Yan, R. S.; Kelly, M. M.; Fang, T.; Tahy, K.; Hwang, W. S.; Jena, D.; Liu, L.; Xing, H. G. Broadband Graphene Terahertz Modulators Enabled by Intraband Transitions. *Nat. Commun.* **2012**, *3*, 780.
- (24) Liang, G.; Hu, X.; Yu, X.; Shen, Y.; Li, L. H.; Davies, A. G.; Linfield, E. H.; Liang, H. K.; Zhang, Y.; Yu, S. F.; Wang, Q. J. Integrated Terahertz Graphene Modulator with 100% Modulation Depth. *ACS Photonics* **2015**, *2* (11), 1559–1566.
- (25) Lee, A. W. M.; Qin, Q.; Kumar, S.; Williams, B. S.; Hu, Q. Real-Time Terahertz Imaging over a Standoff Distance (> 25 Meters). *Appl. Phys. Lett.* **2006**, *89* (14), 141125.

- (26) Lee, A. W. M.; Williams, B. S.; Kumar, S.; Hu, Q.; Reno, J. L. Real-Time Imaging Using a 4.3-THz Quantum Cascade Laser and a 320 X 240 Microbolometer Focal-Plane Array. *IEEE Photonics Technol. Lett.* **2006**, *18* (13-16), 1415–1417.
- (27) Zeng, Y.; Liang, G.; Liang, H.; Mansha, S.; Li, L.; Davies, A. G.; Linfield, E.; Zhang, Y.; Chong, Y.; Wang, Q. Amorphous Random Lasing at Terahertz Frequency. In *Conference on Lasers and Electro-Optics*; Optical Society of America, 2016; p SM2L.5.
- (28) Faist, J.; Capasso, F.; Sivco, D. L.; Sirtori, C.; Hutchinson, A. L.; Cho, A. Y. Quantum Cascade Laser. *Science* (80-.). **1994**, *264*, 553–556.
- (29) Dunbar, L. A.; Moreau, V.; Ferrini, R.; Houdré, R.; Sirigu, L.; Scalari, G.; Giovannini, M.; Hoyler, N.; Faist, J. Design, Fabrication and Optical Characterization of Quantum Cascade Lasers at Terahertz Frequencies Using Photonic Crystal Reflectors. *Opt. Express* **2005**, *13* (22), 8960–8968.
- (30) Jin, C. J.; Meng, X. D.; Cheng, B. Y.; Li, Z. L.; Zhang, D. Z. Photonic Gap in Amorphous Photonic Materials. *Phys. Rev. B* **2001**, *63* (19), 195107.
- (31) Mansha, S.; Yongquan, Z.; Wang, Q. J.; Chong, Y. D. Optimization of TM Modes for Amorphous Slab Lasers. *Opt Express* **2016**, *24* (5), 4890–4898.
- (32) Williams, B. S.; Kumar, S.; Callebaut, H.; Hu, Q.; Reno, J. L. Terahertz Quantum-Cascade Laser at Lambda Approximate to 100 Mu M Using Metal Waveguide for Mode Confinement. *Appl. Phys. Lett.* **2003**, *83* (11), 2124–2126.
- (33) Unterrainer, K.; Colombelli, R.; Gmachl, C.; Capasso, F.; Hwang, H. Y.; Sergent, A. M.; Sivco, D. L.; Cho, A. Y. Quantum Cascade Lasers with Double Metal-Semiconductor Waveguide Resonators. *Appl. Phys. Lett.* **2002**, *80* (17), 3060–3062.
- (34) Zhang, H.; Dunbar, L. A.; Scalari, G.; Houdre, R.; Faist, J. Terahertz Photonic Crystal Quantum Cascade Lasers. *Opt Express* **2007**, *15* (25), 16818–16827.
- (35) Zhang, H.; Scalari, G.; Faist, J.; Dunbar, L. A.; Houdre, R. Design and Fabrication Technology for High Performance Electrical Pumped Terahertz Photonic Crystal Band

Edge Lasers with Complete Photonic Band Gap. *J. Appl. Phys.* **2010**, *108* (9), 93104.

- (36) Zhang, H.; Scalari, G.; Beck, M.; Faist, J.; Houdre, R. Complex-Coupled Photonic Crystal THz Lasers with Independent Loss and Refractive Index Modulation. *Opt Express* **2011**, *19* (11), 10707–10713.
- (37) Diao, Z. L.; Bonzon, C.; Scalari, G.; Beck, M.; Faist, J.; Houdre, R. Continuous-Wave Vertically Emitting Photonic Crystal Terahertz Laser. *Laser Photon. Rev.* **2013**, *7* (5), L45–L50.
- (38) Gottardo, S.; Sapienza, R.; García, P. D.; Blanco, A.; Wiersma, D. S.; López, C. Resonance-Driven Random Lasing. *Nat. Photonics* **2008**, *2* (7), 429–432.
- (39) Garcia, P. D.; Ibisate, M.; Sapienza, R.; Wiersma, D. S.; Lopez, C. Mie Resonances to Tailor Random Lasers. *Phys. Rev. A* **2009**, *80* (1), 13833.
- (40) Noh, H.; Yang, J. K.; Liew, S. F.; Rooks, M. J.; Solomon, G. S.; Cao, H. Control of Lasing in Biomimetic Structures with Short-Range Order. *Phys. Rev. Lett.* **2011**, *106* (18), 183901.
- (41) Belkin, M.; Wang, Q.; Pflügl, C.; Belyanin, A.; Khanna, S. P.; Davies, A. G.; Linfiel, E. H.; Capasso, F. High-Temperature Operation of Terahertz Quantum Cascade Laser Sources. *IEEE J. Sel. Top. Quantum Electron.* **2009**, *15* (3), 952–967.
- (42) Liang, H. K.; Meng, B.; Liang, G. Z.; Tao, J.; Chong, Y. D.; Wang, Q. J.; Zhang, Y. Electrically Pumped Mid-Infrared Random Lasers. *Adv. Mater.* **2013**, *25* (47), 6859–6863.
- (43) Cunningham, P. D.; Valdes, N. N.; Vallejo, F. A.; Hayden, L. M.; Polishak, B.; Zhou, X. H.; Luo, J.; Jen, A. K. Y.; Williams, J. C.; Twieg, R. J. Broadband Terahertz Characterization of the Refractive Index and Absorption of Some Important Polymeric and Organic Electro-Optic Materials. *J. Appl. Phys.* **2011**, *109* (4), 2–7.
- (44) Pavanello, F.; Garet, F.; Kuppam, M. B.; Peytavit, E.; Vanwolleghe, M.; Vaurette, F.; Coutaz, J. L.; Lampin, J. F. Broadband Ultra-Low-Loss Mesh Filters on Flexible Cyclic Olefin Copolymer Films for Terahertz Applications. *Appl. Phys. Lett.* **2013**, *102* (11), 111114.

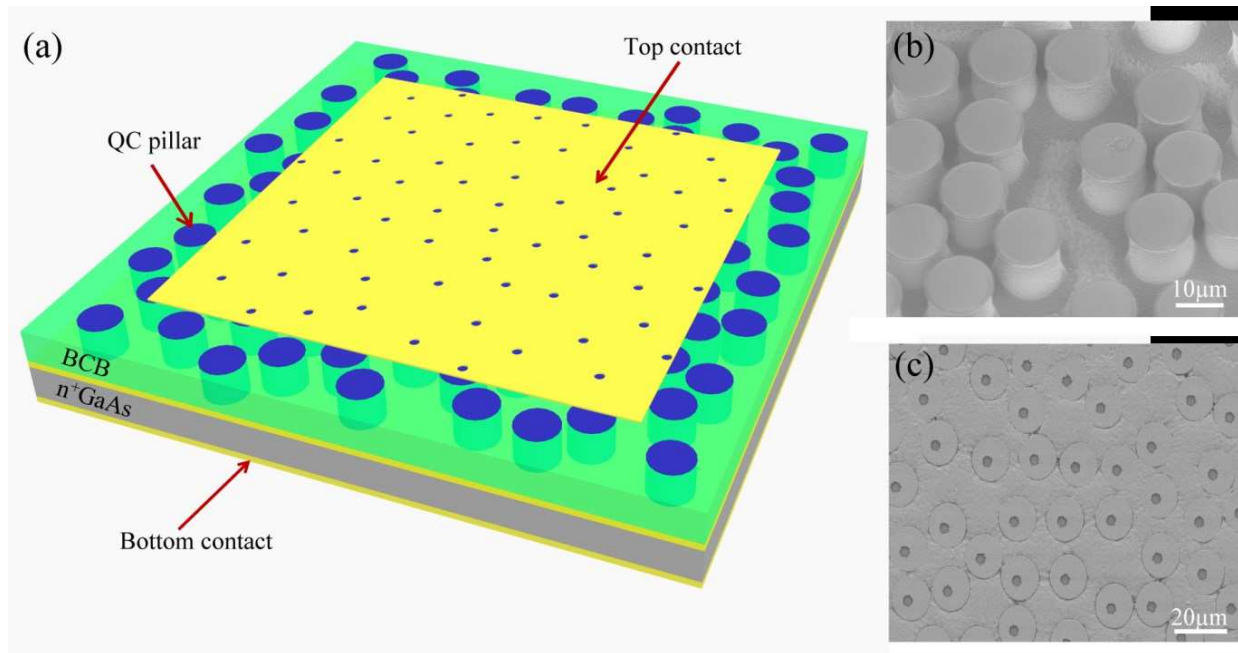


Fig. 1. Terahertz random laser with two-dimensional (2D) amorphous pillar lattice. (a) 3D schematic diagram of a surface-emitting terahertz random quantum cascade laser. (b) Scanning electron microscope (SEM) images of the quantum cascade (QC) pillars at an oblique angle after inductively coupled plasma (ICP) dry etching, and (c) the surface of the finished device. The pillar height is 10 μm . Holes of radius 1.5 μm are etched into the top contact plate, at the pillar centers, to allow for surface emission.

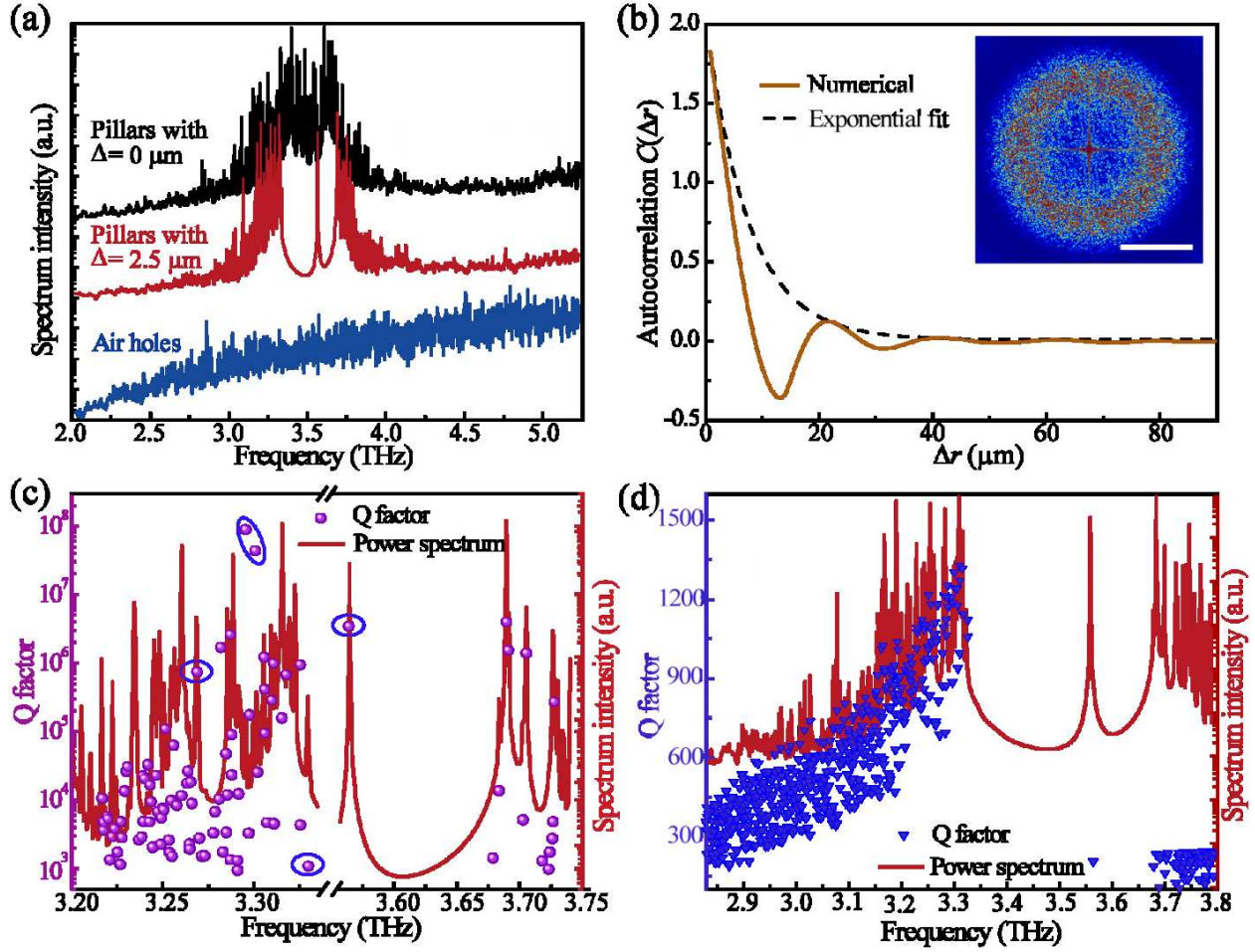


Fig. 2. Spectral and spatial analysis of the random structures. (a) Simulated power spectra (vertically offset for clarity) of 2D structures with a pillar radius $6.4 \mu\text{m}$, filling fraction (FF) 36.5%, and a total device area of $1000 \mu\text{m} \times 1000 \mu\text{m}$. The black and red curves correspond to minimum edge separations of $\Delta = 0 \mu\text{m}$ and $\Delta = 2.5 \mu\text{m}$, respectively. The refractive index contrast is approximately 3.6 (QC pillar): 1.58 (BCB). The blue curve corresponds to a random air-hole structure, without pillars. (b) Ensemble averaged spatial autocorrelation function $C(\Delta r)$ for structures with $\Delta = 2.5 \mu\text{m}$; the black dashed curve is an exponential fit. The inset shows the spatial Fourier transform of the structure, where the scale bar is $2\pi/a$; a is the average center-to-center distance between the pillars. (c) Power spectrum (red curve) and modal in-plane Q factors (purple dots) in the vicinity of the gap. The frequency region 3.34–3.55 THz has been omitted to show the Q factors at the edges of the gap clearly. Material losses are neglected. The modes highlighted by the blue ellipses correspond to the intensity distribution plots in Fig. 3a. (d) Modal

Q factors (blue triangles) with the BCB loss of $\sim 10.9 \text{ cm}^{-1}$ taken into account. The power spectrum is overlaid as a guide to the eye. Note that the metallic loss of the double metal waveguide and the vertical surface emission loss from apertures are not considered for this Q factor calculation. A full-structure 3D simulation will result in lower Q factors accordingly.

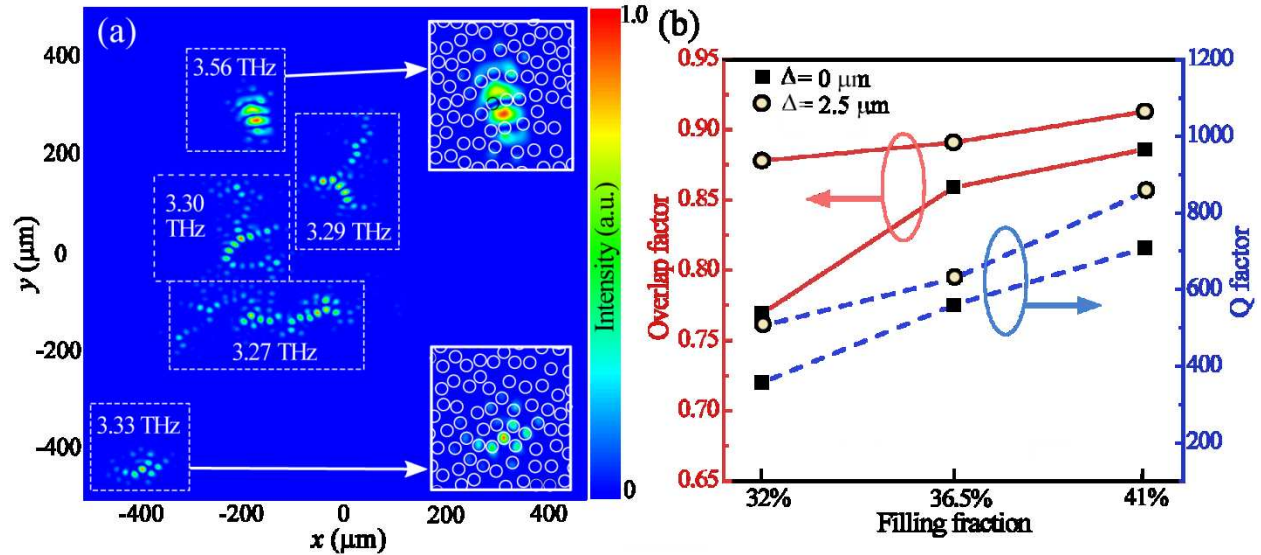


Fig. 3. Optical mode distributions of the random structures. (a) Field intensity distributions of the modes highlighted by the blue ellipses in Fig. 2c. The mode intensities have been normalized for clarity. All modes are localized. The field intensity distributions of the two modes at 3.33 THz and 3.56 THz are amplified and shown as insets. As indicated in the insets, the modes near the bottom of the gap (at 3.33 THz) are mainly concentrated in the pillars, while modes near the top of the gap (at 3.56 THz) are mainly concentrated in the BCB. (b) Overlap factor and in-plane Q factors, with BCB losses accounted for, averaged over 100 modes with field energy mainly confined in the QC pillars for different FFs. The pillar radius is $6.4 \text{ }\mu\text{m}$, and the total device area is $1000 \text{ }\mu\text{m} \times 1000 \text{ }\mu\text{m}$. Squares indicate structures with $\Delta = 0 \text{ }\mu\text{m}$, and circles indicate structures with $\Delta = 2.5 \text{ }\mu\text{m}$.

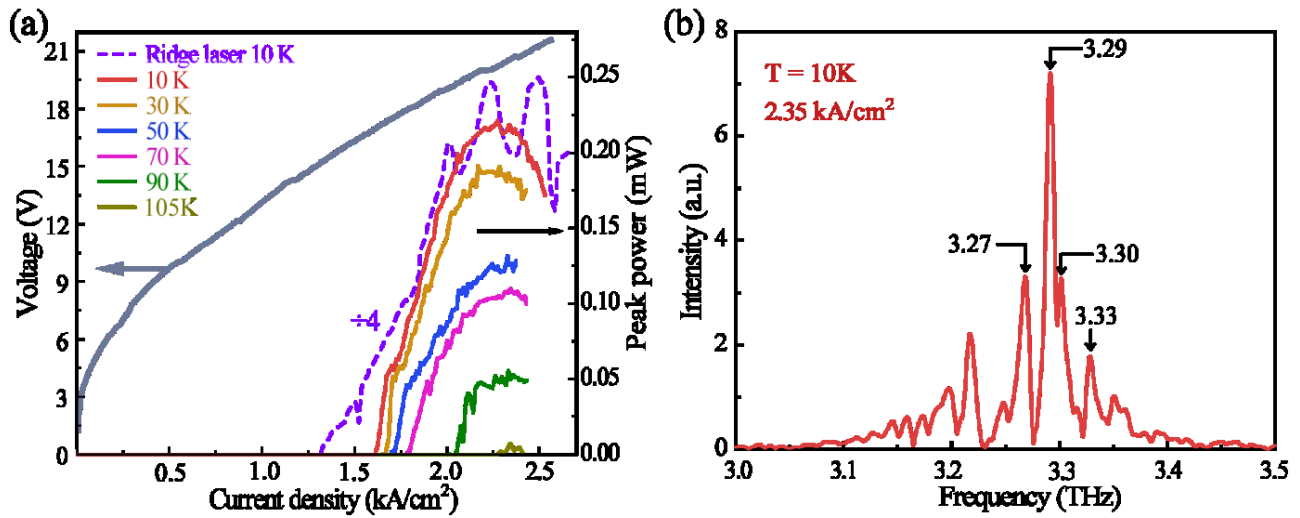


Fig. 4. Emission characteristics of random QCLs. (a) LIV curve of a random QCL with pillar radius of $6.4 \mu\text{m}$, $\text{FF} = 36.5\%$, and $\Delta = 2.5 \mu\text{m}$. The light-current curve of a ridge laser at 10 K is plotted for comparison (violet dashed lines); its intensity is reduced by a factor of four for clarity. (b) Emission spectrum of the same device at the rollover current density, measured at 10 K. The spectral resolution is 0.2 cm^{-1} . The spectral peaks occur between 3.1–3.4 THz, in agreement with the simulation results shown in Fig. 2d and Fig. 3a.

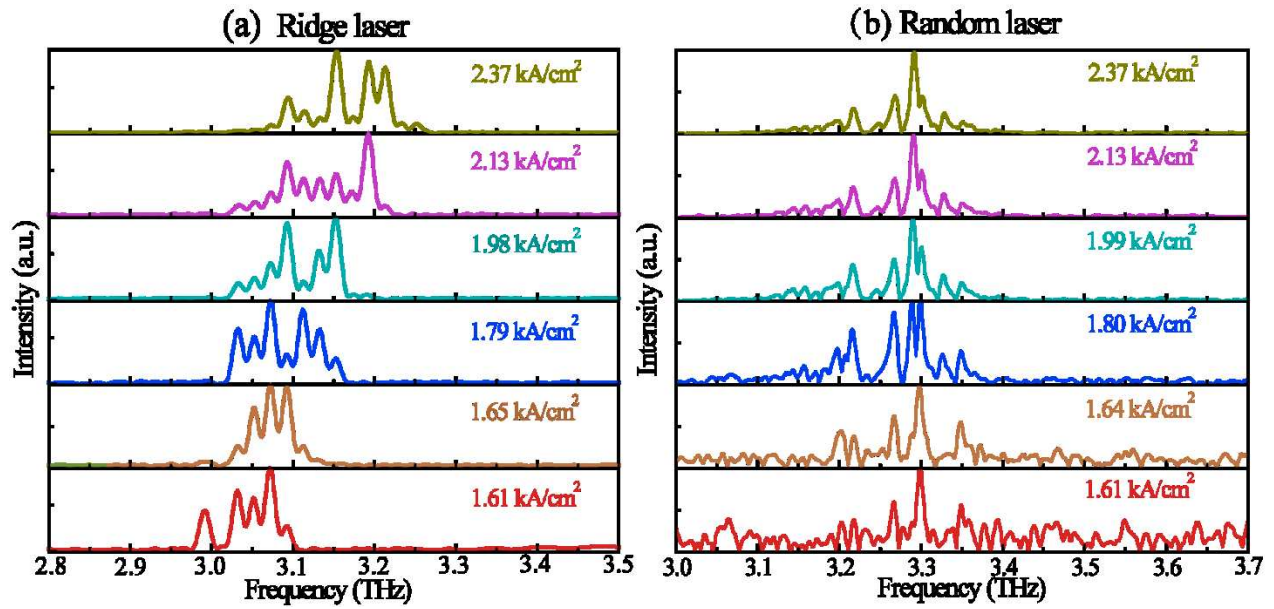


Fig. 5. Comparison of the emission spectra between a random QCL and a ridge QCL. (a) Emission spectra of a double-metal waveguide ridge laser (width = 106 μm and length = 2 mm) at different pumping current densities (the spectra are selected to better present the gradual blue shift of emission peaks). (b) Emission spectra of a random QCL (pillar size 6.4 μm , FF = 36.5%, $\Delta = 2.5 \mu\text{m}$) at different pumping current densities. The spectral resolution is 0.2 cm^{-1} for the random laser, and 0.5 cm^{-1} for the ridge laser, respectively.

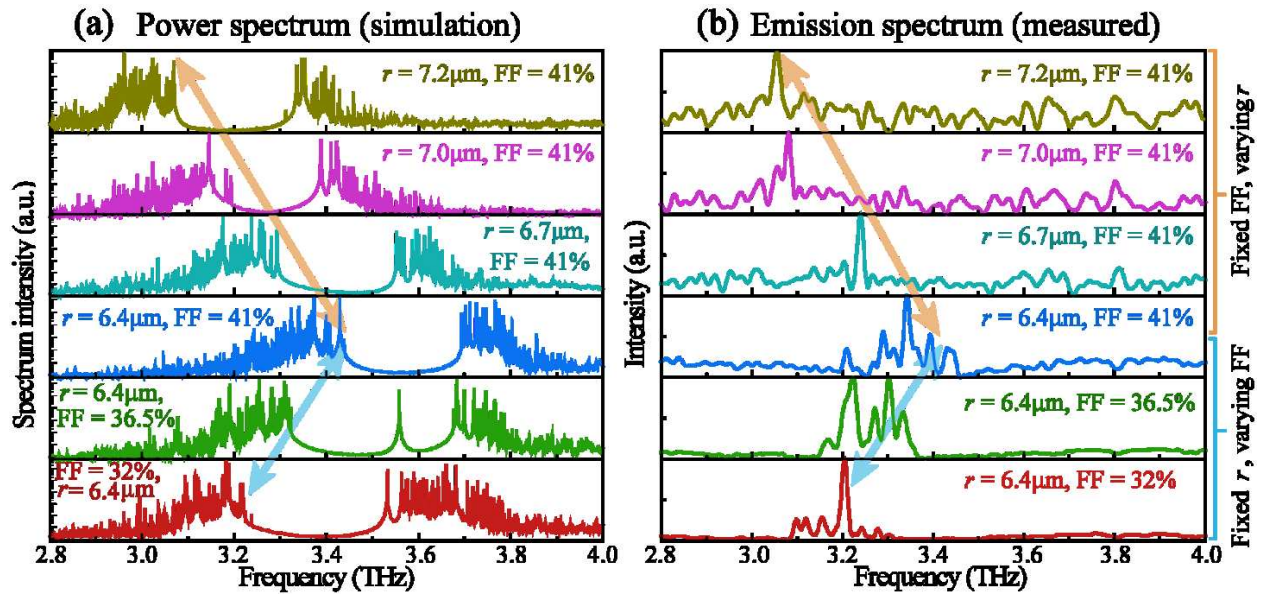


Fig. 6. Emission tuning of the random structures. (a) Calculated power spectra for different random structures, with device parameters indicated in the figure, without considering the BCB waveguide losses. The arrows indicate the trend of the band-edge shift with varying parameters. (b) Measured emission spectra of the fabricated random QCL devices. The asymmetric profile of emission spectra is caused by the fact that the higher frequency band edge modes have a larger overlap with the BCB waveguide (thus with higher losses) compared to lower frequency band edge modes. See Fig. 2d for the simulation results.